Supporting Information

Influence of Precursor Type on NMC811 Cathode Material Properties: Insights from Spray Pyrolysis Synthesis and In-Situ XRD Analysis

Manar Almazrouei,[a,b,*] Farheen Sayed,[c] Dingyu Hou,[d] Clare P. Grey,[c] Kai Luo,[d] Simone Hochgreb,[a] Michael De Volder,[a] Adam Boies[a,e,*]

[a]Department of Engineering, University of Cambridge, Cambridge CB2 1PZ, UK

[b]Department of Mechanical and Aerospace Engineering, United Arab Emirates University, Al Ain, Abu Dhabi, UAE

[c]Yusuf Hamied Department of Chemistry, University of Cambridge, Cambridge CB2 1EW, UK

[d]Department of Mechanical Engineering, University College London, London WC1E 7JE, UK

[e]Department of Mechanical Engineering, Stanford University, Stanford, CA 94305, USA

*Corresponding authors: manar.almazrouei@uaeu.ac.ae, aboies@stanford.edu

1. Literature Survey: Spray Pyrolysis and Annealing Conditions

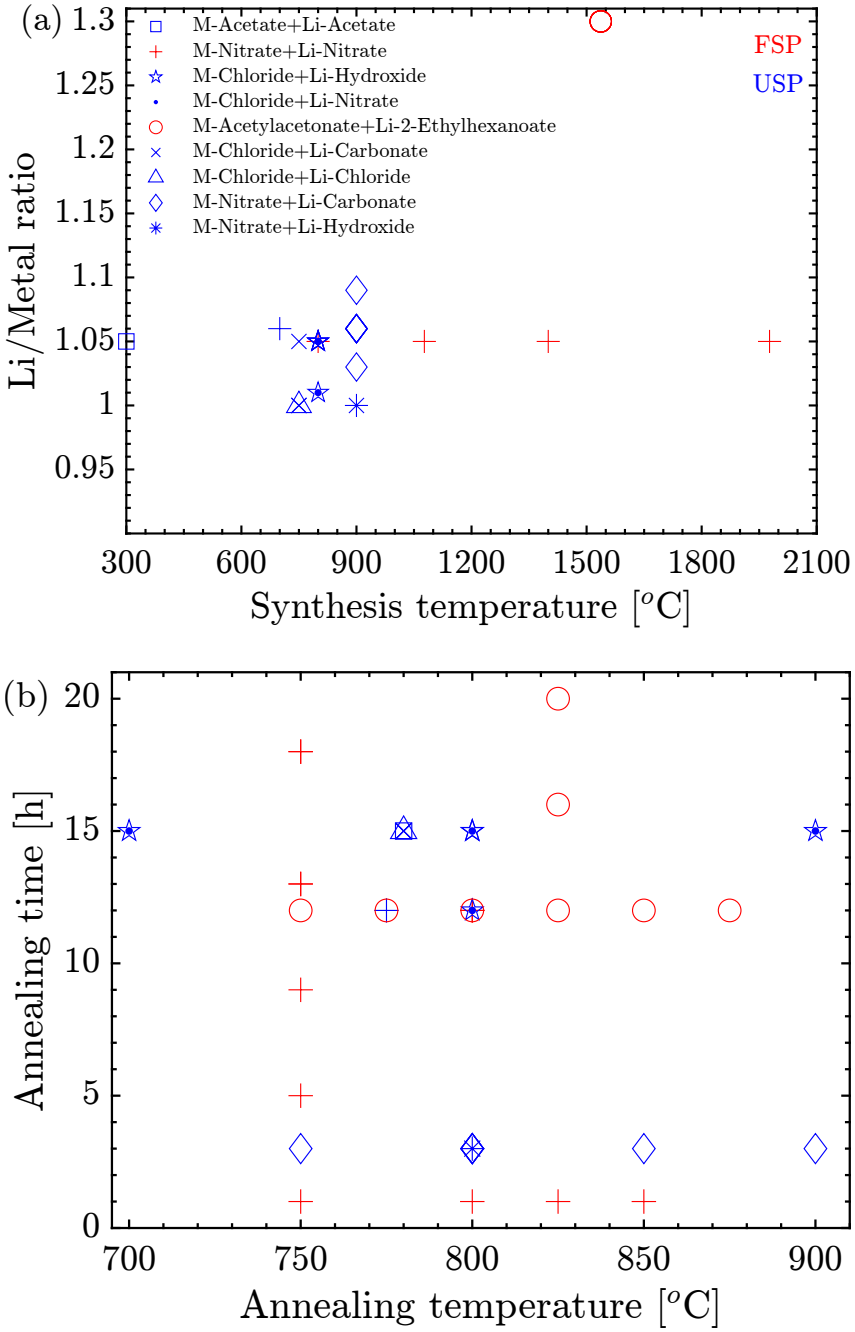

Figure S1: Survey of aerosol (SP/FSP) conditions reported for NMC811: (a) reactor synthesis temperatures and precursor details; (b) post-synthesis annealing temperatures and durations. [1–16]

Analysis of prior aerosol syntheses shows that nitrates and chlorides are the predominant transition-metal (TM) sources, while LiOH, Li_2CO_3, LiCl, and $LiNO_3$ are the most common lithium sources. Ultrasonic spray pyrolysis (USP) is typically used to form TM oxides first, with lithium added subsequently via a solid-state step. [2,4–6,8,9,12] By contrast, flame spray pyrolysis (FSP) often dissolves Li directly into the precursor solution, enabling single-pass formation of lithiated products prior to post-anneal. [7,10,13–16] Reported aerosol (SP/FSP) settings span reactor temperatures of 600 °C–1000 °C and post-synthesis anneals of 700 °C–900 °C; see Figure S1 for the compiled conditions. The most frequent Li:TM (molar) ratios for NMC811 aerosols are 1.00, 1.05, and 1.10.

Several studies have examined how synthesis parameters impact NMC performance. For USP, Ju *et al.* [3] varied the Li_2CO_3 fraction in a mixed nitrate/acetate precursor for $LiNi_{0.8}Co_{0.15}Mn_{0.05}O_2$, linking

lithium excess to phase purity and electrochemistry. Wang *et al.*[12] adjusted the $LiNO_3$ content when pairing USP-made TM oxides with lithium sources to form $LiNi_{0.9}Co_{0.055}Mn_{0.045}O_2$, showing grain-size/kinetic trade-offs. For NMC811 produced via USP, reactor set-points of 750 °C and 800 °C are most commonly reported.

Annealing windows have likewise been mapped. Temperatures of 750 °C, 780 °C, and 800 °C dominate both single- and two-step anneals (Figure S1b). For USP precursors, Ju *et al.*[3] explored 700 °C to 900 °C for $LiNi_{0.8}Co_{0.15}Mn_{0.05}O_2$, and Zhu *et al.*[8] employed a two-step sequence (450 °C pre-treatment followed by 700 °C to 900 °C) for NMC811. For FSP powders, Liang *et al.*[10] used single-step anneals across 750 °C to 875 °C, while Zhang *et al.*[14] applied a two-step protocol (450 °C then 750 °C to 850 °C). Collectively, these reports establish practical synthesis/anneal ranges and Li:TM ratios against which the present work is benchmarked.

2. Thermal Behavior of Precursor Salts

To better understand the thermal decomposition behavior of the precursors used in spray pyrolysis synthesis, thermogravimetric analysis (TGA) was performed. This helps identify optimal synthesis conditions and supports precursor selection rationale.

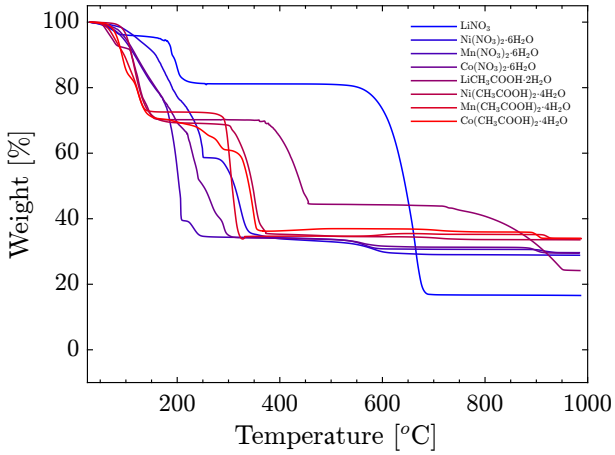

Figure S2: TGA assessment of lithium and other metals utilized as precursors for layered oxide cathode materials.

3.Droplet Drying and Solute Diffusion

To validate the influence of the metal source type on particle morphology, we utilized diffusion coefficient data for $Ni(NO_3)_2$ and $Ni(CH_3COO)_2$ from molecular dynamics simulations conducted. The simulations maintained 300 Ni^{2+} ions with 600 anions (NO_3^- or CH_3COO^-). Different water-to-solute ratios (WSR) were achieved by varying the number of H_2O molecules.

At WSR = 50, the water volume was calculated as:

$$V_{H_2O} = \frac{15000 \times M_{H_2O}}{N_A \times \rho_{H_2O}} \tag{S1}$$

where M_{H_2O} = 18 g/mol, N_A is Avogadro's number, and ρ_{H_2O} = 1000 kg/m^3. This yielded a precursor concentration of 1.1 mol/L. Figure S3 shows the diffusion coefficients for Ni^{2+} in both solutions.

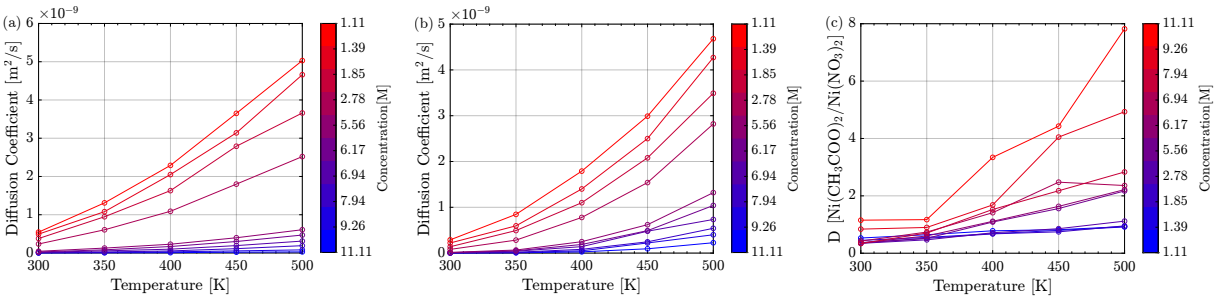

Figure S3: Diffusion coefficient of Ni^{2+} in (a) $Ni(NO_3)_2$ and (b) $Ni(CH_3COO)_2$ solutions at different precursor temperatures and concentrations alongside the (c) diffusion coefficient ratios between the two different precursor types.

The diffusion coefficients increase with temperature following the Stokes-Einstein equation:

$$D = \frac{k_B T}{6\pi\eta a} \tag{S2}$$

where k_B is Boltzmann's constant, T is temperature, η is viscosity, and a is particle radius.[17] Higher concentrations reduce the diffusion coefficient, and nitrate solutions generally show higher diffusion coefficients than acetate at lower concentrations (up to 2.8 M) and higher temperatures (up to 450 K).

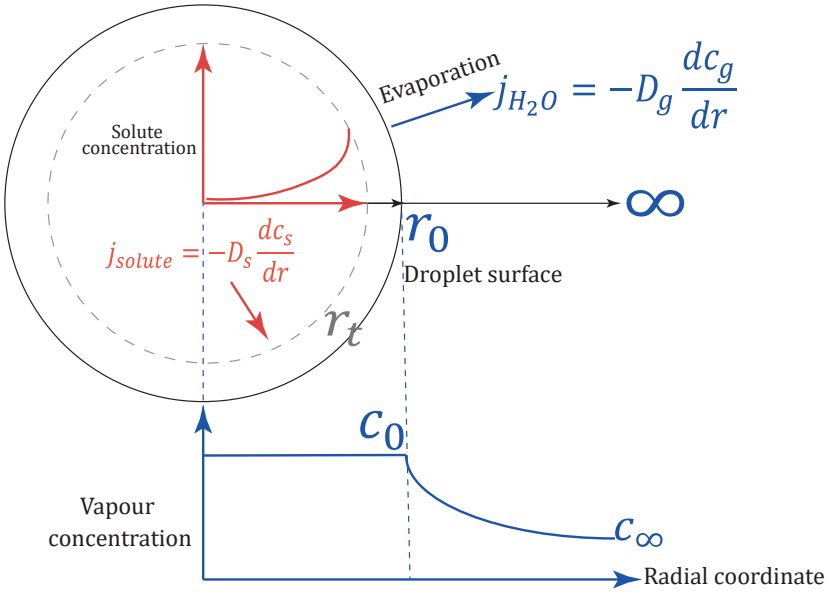

Figure S4: Conceptual schematic of the droplet drying process and solute diffusion.

We developed a droplet drying model to understand surface enrichment during evaporation. The vapor flux follows Fick's first law:

$$j = -D\frac{dc}{dr} \tag{S3}$$

Through mass conservation and integration, this leads to Maxwell's equation:

$$I = -\frac{dm}{dt} = -4\pi r D_g(c_0 - c_\infty) \tag{S4}$$

Substituting the ideal gas law and droplet geometry yields the r^2-law:

$$r^2 = r_0^2 - 2\frac{D_g M}{\rho_p RT}(p_0 - p_\infty)t \tag{S5}$$

where D_g is vapor diffusion coefficient, M is molar mass, and p_0, p_∞ are vapor pressures. Figure S5 shows droplet evaporation kinetics under various conditions.

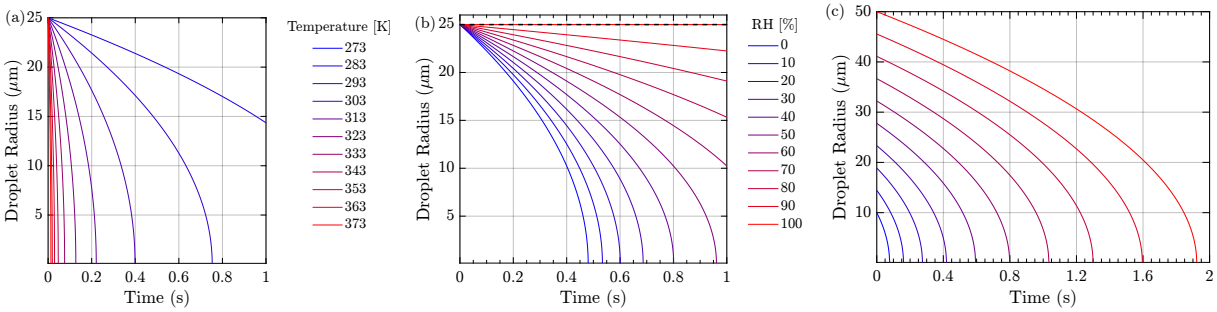

Figure S5: Pure water droplet evaporation at various conditions: (a) 25 µm droplet radius at RH=0% and various temperatures in the range of 273-373 K, (b) at different relative humidity (RH), and fixed temperature of 300 K, (c) with varying initial sizes at 300K and RH=0%.

For solute diffusion during evaporation, we used Fick's second law in spherical coordinates:

$$\frac{\partial c}{\partial t} = D_s\left(\frac{\partial^2 c}{\partial r^2} + \frac{2}{r}\frac{\partial c}{\partial r}\right) \tag{S6}$$

The model incorporated Raoult's law for vapor pressure depression and was solved numerically using MATLAB. Key findings are shown in Figure S6.

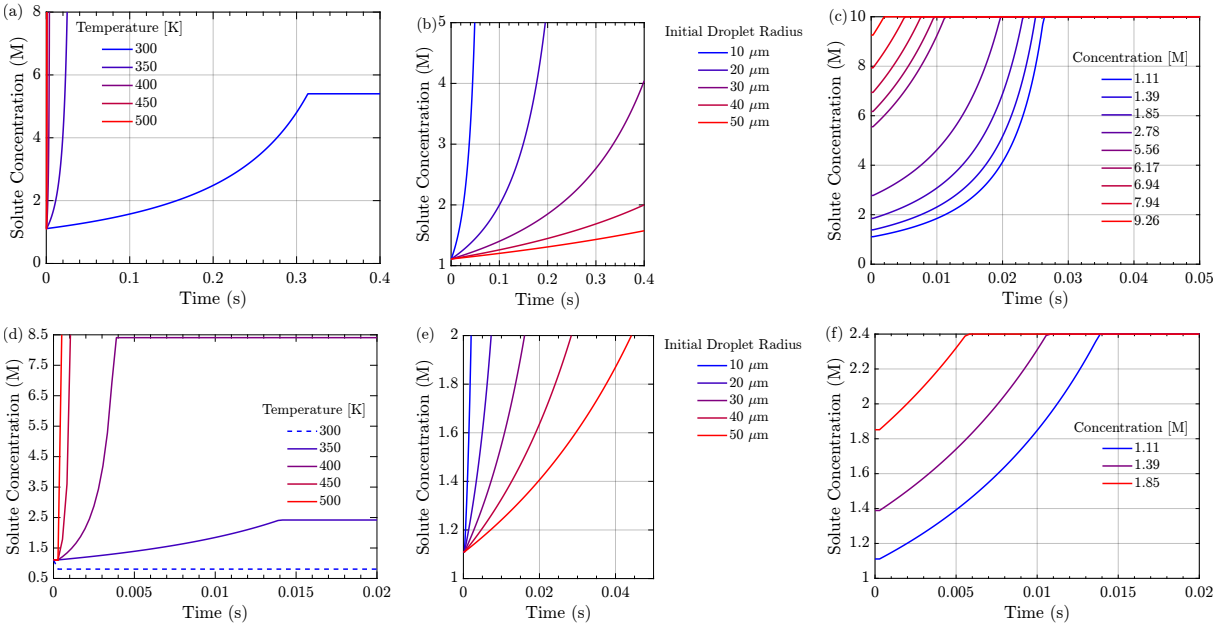

Figure S6: Effect of droplet's temperature (a,d), size (b,e), and initial concentration (c,f) on the solute diffusion of Ni^{2+} in $Ni(NO_3)_2$ (a-c) and $Ni(CH_3COO)_2$ (d-f) solutions.

The different solubility limits—5.4 M for $Ni(NO_3)_2$ at 298 K versus 0.81 M for $Ni(CH_3COO)_2$—drive distinct precipitation behaviors.[7,18] Acetate droplets reach supersaturation and precipitate much faster. For example, a 25 µm nitrate droplet at 350 K with 1.11 M concentration precipitates in 0.02 s, while an equivalent acetate droplet precipitates in 0.014 s. These results explain the morphological differences observed in TEM analysis: nitrate particles form thicker shells due to slower precipitation, while acetate particles develop thin, wrinkled shells from rapid surface precipitation.

4. Morphology of As-Synthesized NMC811 Particles

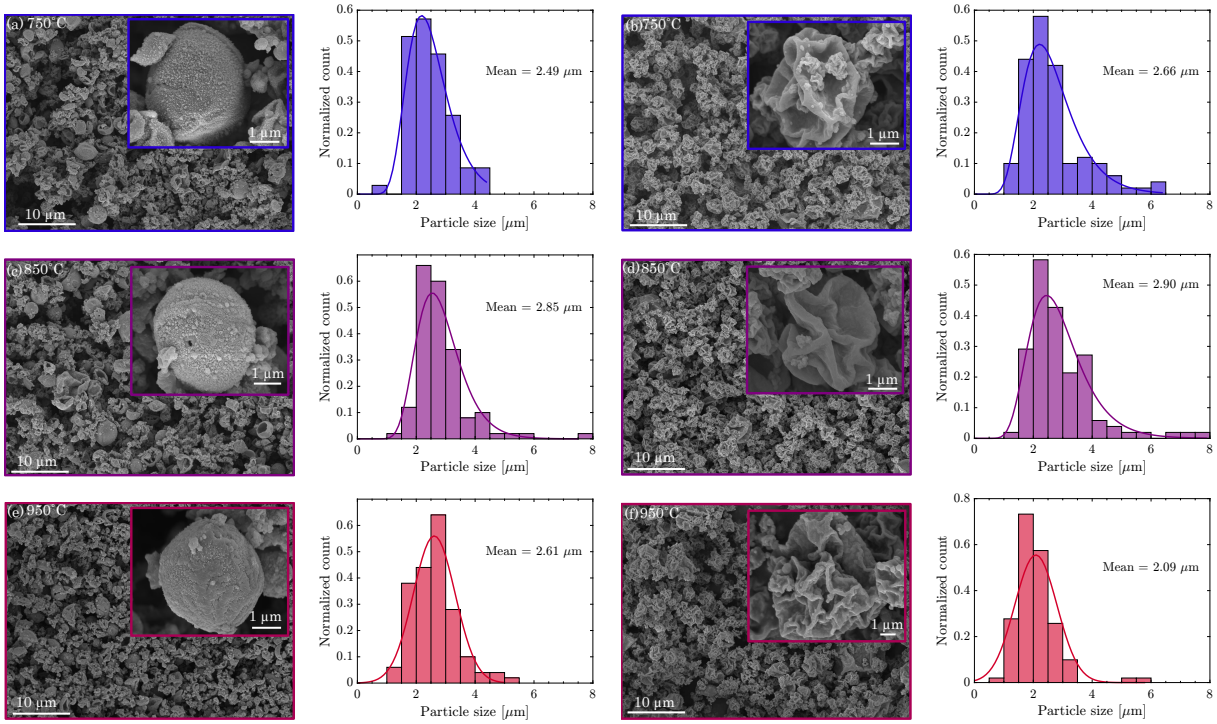

Figure S7: Morphological characterisation of NMC811 particles synthesised from nitrate (left) and acetate (right) precursors at (a,b) 750°C, (c,d) 850°C, and (e,f) 950°C. SEM images show lower (10 µm scale bar) and higher (1 µm scale bar, inset) magnifications. Corresponding particle size distributions are presented adjacent to each SEM image set.

5. Structural Evolution via Rietveld Refinement

Table S1: Rietveld refinement parameters for annealed NMC811 particles showing evolution of lattice parameters and cation ordering with annealing time

Precursor	**Time (h)**	**a (Å)**	**c (Å)**	**c/a**	**V (Å^3)**	**Li/Ni mixing (%)**	**R_{wp} (%)**
Nitrate precursor - Annealed at 775°C							
Nitrate	0.5	2.8661(2)	14.201(1)	4.954	101.02	3.2(3)	8.4
	1	2.8663(2)	14.204(1)	4.955	101.05	3.1(3)	8.2
	3	2.8667(1)	14.210(1)	4.956	101.13	2.8(2)	7.9
	5	2.8670(1)	14.213(1)	4.957	101.18	2.7(2)	7.8
	10	2.8672(1)	14.215(1)	4.957	101.21	2.9(2)	8.0
	15	2.8669(2)	14.211(1)	4.956	101.16	3.3(3)	8.3
Acetate precursor - Annealed at 725°C							
Acetate	0.5	2.8642(3)	14.163(2)	4.945	100.62	5.8(4)	9.2
	1	2.8645(3)	14.168(2)	4.946	100.68	5.5(4)	9.0
	3	2.8648(2)	14.175(2)	4.948	100.76	4.9(3)	8.8
	5	2.8655(2)	14.187(1)	4.951	100.90	4.1(3)	8.5
	10	2.8663(1)	14.203(1)	4.954	101.04	3.2(2)	8.1
	15	2.8665(1)	14.206(1)	4.955	101.08	3.0(2)	8.0
	20	2.8664(2)	14.204(1)	4.954	101.06	3.3(3)	8.2

6. Morphological Evolution During Annealing

The morphological evolution during annealing is shown in Figures S8 and S9. Particle sizes were measured from at least 50 particles using ImageJ. Nitrate-derived particles annealed at 775°C transformed from secondary shell-like structures (2.7 µm average) to primary crystalline particles. The average primary particle size increased from 0.3 µm after 1 h to 0.7 µm after 15 h annealing. Extended annealing produced aggregated structures requiring mechanical processing for electrode preparation, similar to previous flame reactor [7,15] and spray pyrolysis studies. [3,11]

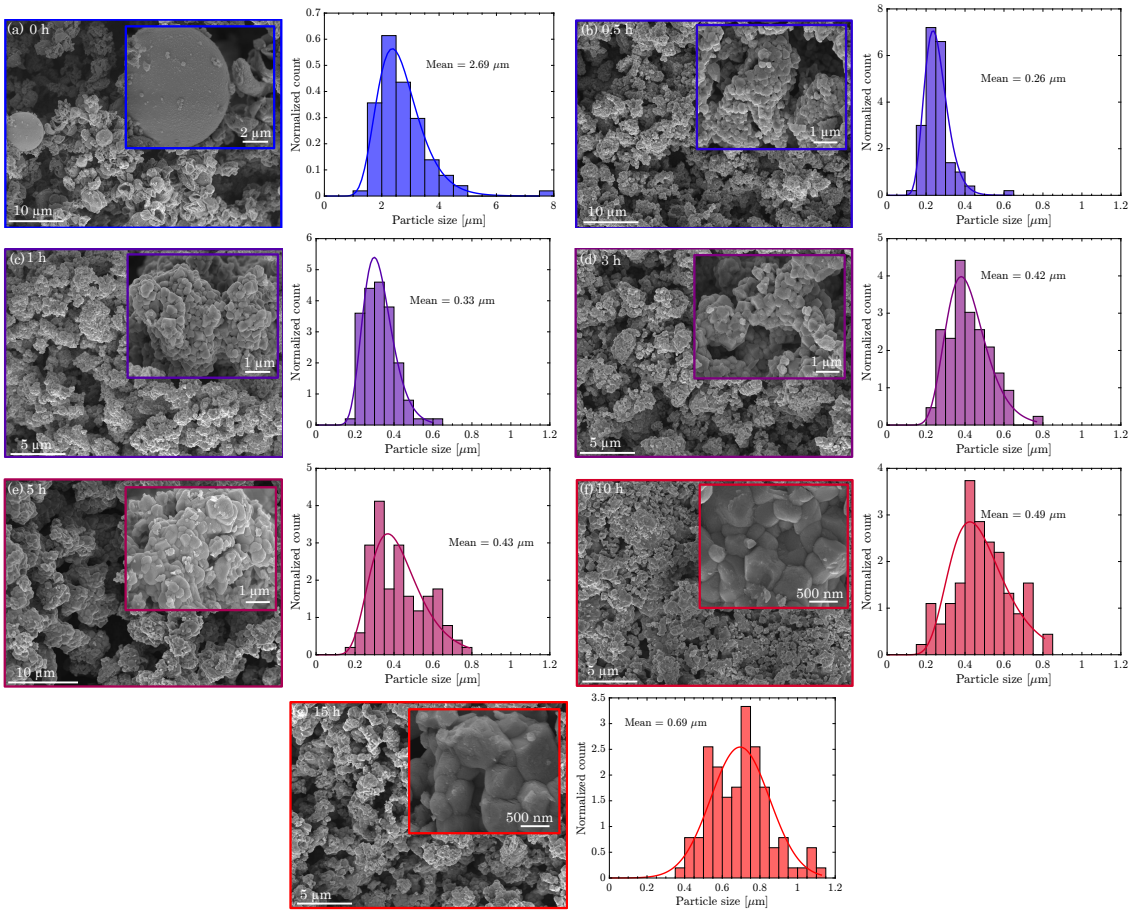

Figure S8: SEM micrographs and particle size distributions of NMC811 particles synthesized at 900°C and annealed at 775°C using nitrate precursors. Annealing times: (a) 0 h, (b) 0.5 h, (c) 1 h, (d) 3 h, (e) 5 h, (f) 10 h, and (g) 15 h. Each panel shows a lower magnification image (left, scale bar 10 µm), higher magnification inset (top left, scale bar 1 µm for a-e, 500 nm for f-g), and corresponding size distribution histogram (right).

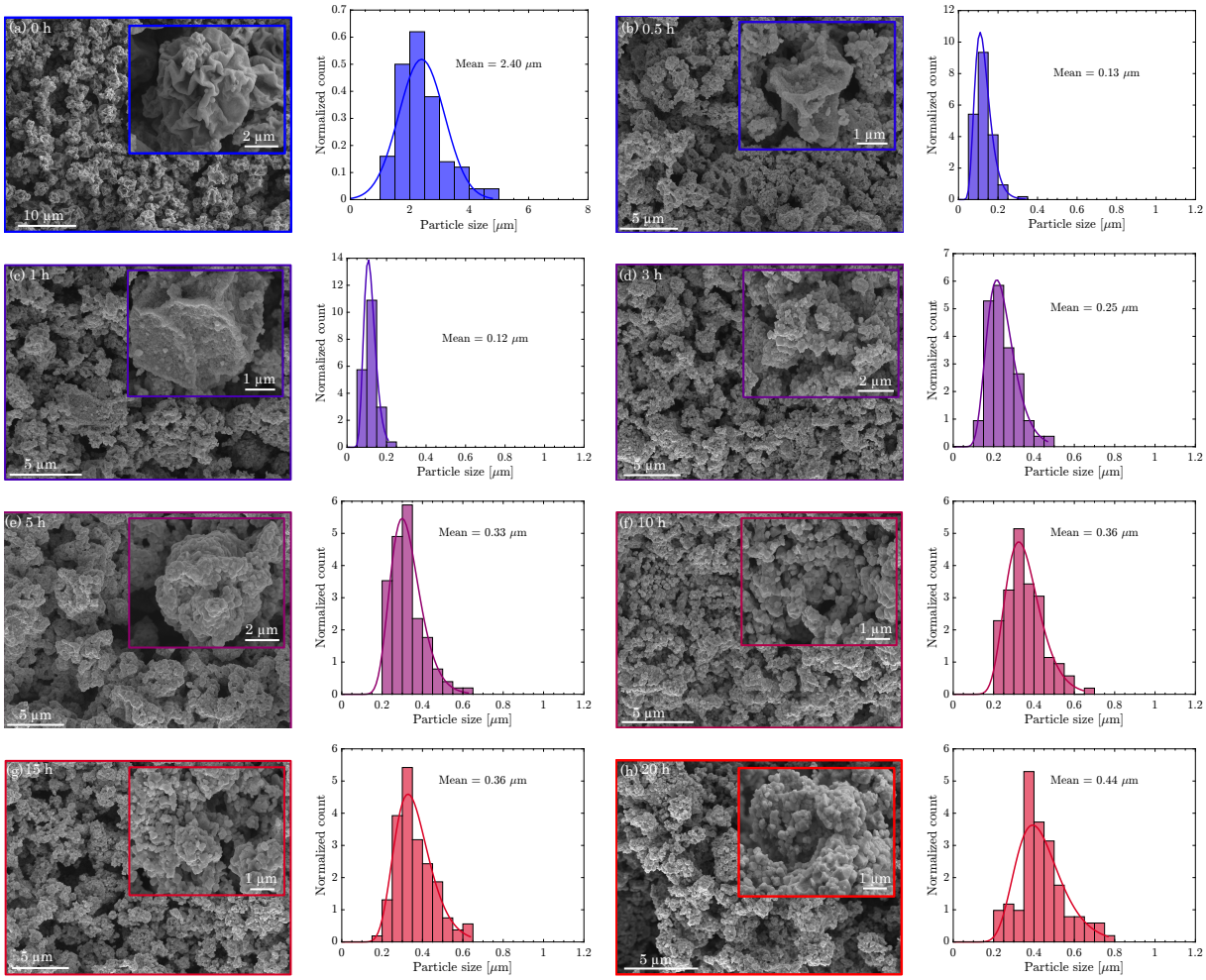

Figure S9: Morphological evolution and particle size distribution of NMC811 particles synthesized from acetate precursors. SEM micrographs (left in each pair) and corresponding particle size distributions (right) for samples annealed at 725°C for various durations: (a,b) 0 h, (c,d) 0.5 h, (e,f) 1 h, (g,h) 3 h, (i,j) 5 h, (k,l) 10 h, (m,n) 15 h, and (o,p) 20 h. All samples were initially synthesized at 900°C. SEM images show both lower (main image, scale bar 10 µm) and higher magnification (inset, scale bar 1 µm) views. Particle size distributions were obtained from analysis of lower magnification SEM images. The evolution of particle morphology and size distribution illustrates the impact of annealing duration on NMC811 particle characteristics.

Acetate-derived particles annealed at 725°C maintained their wrinkled morphology longer. Primary particles grew from 0.12 µm (1 h) to 0.4 µm (20 h), with most growth occurring in the first 5 hours. Unlike nitrate particles, extended annealing did not produce aggregated clusters requiring breaking. This structure matches that reported by You et al.[1] for acetate-derived NMC811 annealed at 780°C for 15 h.

7. Surface Chemistry Characterization via XPS

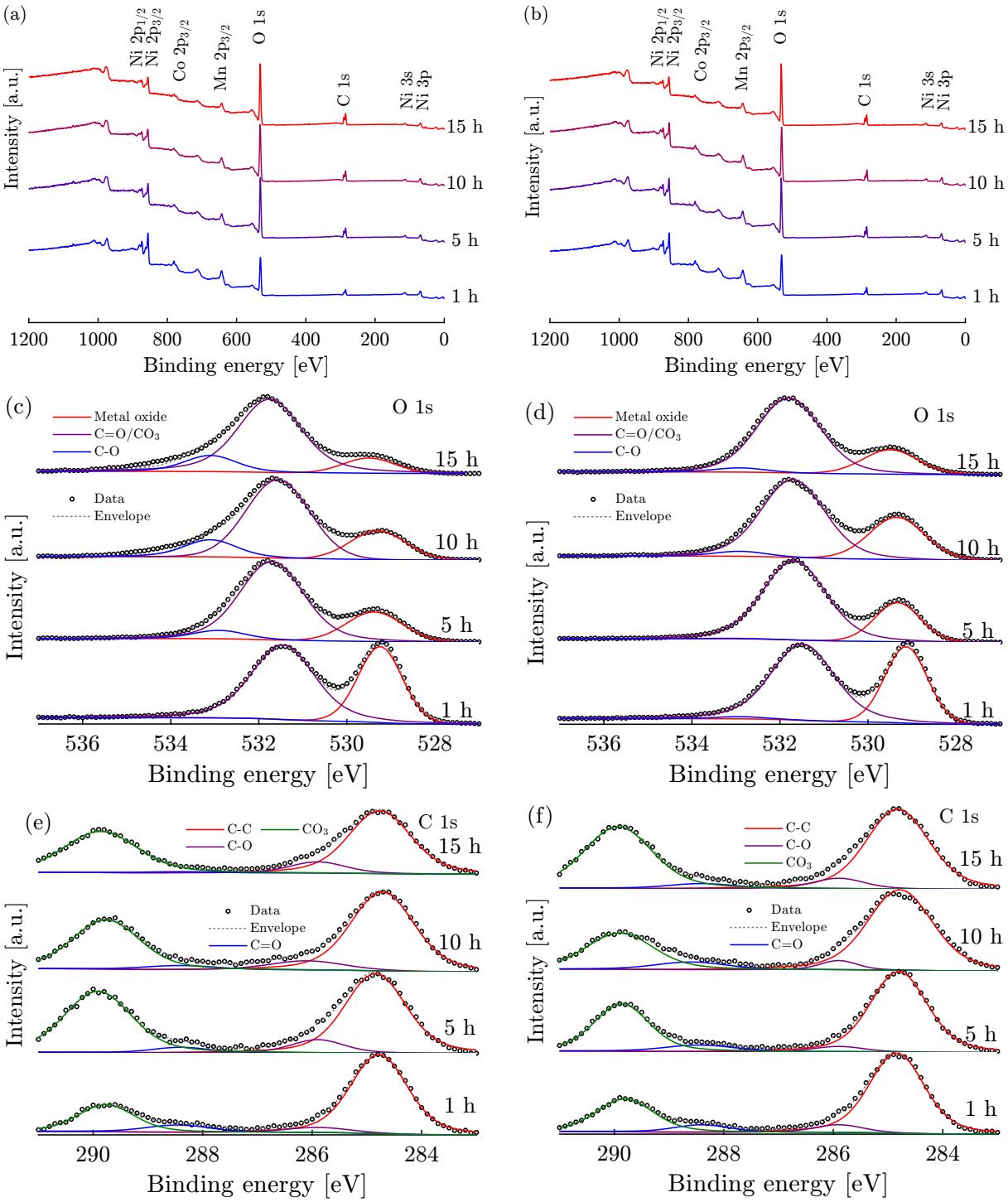

Figure S10: XPS characterization of NMC811 cathode materials synthesized from different precursors and subjected to various annealing durations. (a, b) Survey scans, (c, d) high-resolution O 1s spectra, and (e, f) high-resolution C 1s spectra. Left column (a, c, e): samples from nitrate precursors, synthesized at 900°C and annealed at 775°C. Right column (b, d, f): samples from acetate precursors, synthesized at 900°C and annealed at 725°C. Each spectrum shows data for annealing durations of 1, 5, 10, and 15 h, progressing from bottom to top.

References

[1] B. You, J. Sun, Y. Jing, G. Yan, H. Guo, Z. Wang, D. Wang, W. Peng, Q. Li and J. Wang, *ACS Applied Materials & Interfaces*, 2023, **15**, 14587–14595.

[2] S. H. Ju and Y. C. Kang, *Journal of power sources*, 2008, **178**, 387–392.

[3] S. H. Ju and Y. C. Kang, *Ceramics International*, 2009, **35**, 1633–1639.

[4] T. Li, X. Li, Z. Wang and H. Guo, *Journal of Power Sources*, 2017, **342**, 495–503.

[5] Y. Li, X. Li, Z. Wang, H. Guo and J. Wang, *Journal of energy chemistry*, 2018, **27**, 447–450.

[6] Y. Li, X. Li, Z. Wang, H. Guo, T. Li, K. Meng and J. Wang, *Materials Chemistry Frontiers*, 2018, **2**, 1822–1828.

[7] C. Abram, J. Shan, X. Yang, C. Yan, D. Steingart and Y. Ju, *ACS Applied Energy Materials*, 2019, **2**, 1319–1329.

[8] J. Zhu, J. Zheng, G. Cao, Y. Li, Y. Zhou, S. Deng and C. Hai, *Journal of Power Sources*, 2020, **464**, 228207.

[9] S. Wang, J. Zhu, Y. Li, G. Cao, Y. Chen, D. Zhang, Z. Tan, J. Yang, J. Zheng and H. Li, *Journal of Electroanalytical Chemistry*, 2021, **888**, 115200.

[10] Y. Liang, K. Ku, Y. Lin, L. Yu, J. Wen, E. Lee, J. Libera and J. Lu, *ACS Applied Materials & Interfaces*, 2021, **13**, 26915–26923.

[11] K. Ku, S.-B. Son, J. Gim, J. Park, Y. Liang, A. Stark, E. Lee and J. Libera, *Journal of Materials Chemistry A*, 2022, **10**, 288–295.

[12] J. Wang, X. Lu, Y. Zhang, J. Zhou, J. Wang and S. Xu, *Journal of Energy Chemistry*, 2022, **65**, 681–687.

[13] Y. Lin, C. M. Abram, X. Shi, I. G. McKendry, Z. Wang, H. Zhong, H. Zhao, X. Yang, B. E. Koel, C. Yan *et al.*, *ACS Applied Energy Materials*, 2022, **5**, 10751–10757.

[14] J. Zhang, V. L. Muldoon and S. Deng, *Journal of Power Sources*, 2022, **528**, 231244.

[15] C. Yan, X. Yang, H. Zhao, H. Zhong, G. Ma, Y. Qi, B. E. Koel and Y. Ju, *Proceedings of the Combustion Institute*, 2021, **38**, 6623–6630.

[16] J. Zhang, V. L. Muldoon and S. Deng, *Proceedings of the Combustion Institute*, 2023, **39**, 1165–1173.

[17] J. F. Robinson, F. K. Gregson, R. E. Miles, J. P. Reid and C. P. Royall, *The Journal of Chemical Physics*, 2020, **152**, year.

[18] A. Apelblat and E. Manzurola, *The Journal of Chemical Thermodynamics*, 1999, **31**, 1347–1357.